ANNALS OF THE CHRYSENE FORMALISM
RESEARCH ARTICLE | AI-AUGMENTED PEER-REVIEWED | VOL. 1, NO. 1 | SEPTEMBER 2026

Directional Excited-State Polarization in a 3,6,9,12-Connected Rectangular Chrysene Network: A Range-Separated Fragment Comparison with a Dibenzochrysene Benchmark

Charles D. Schaper, Ph.D.
Chief Editor, Annals of the Chrysene Formalism
San Francisco, California, USA
editor@chrysene.com

Abstract

A central question for chrysene-based artificial-photosynthetic materials is whether visible-light excitation can produce spatially directed electronic response rather than absorption alone. We examine a finite fragment representing the longer C12–C6 direction of a 3,6,9,12-connected rectangular substituted-chrysene network and compare it with a finite fragment derived from a reported dibenzochrysene (DBC) photocatalytic framework. Ground states were calculated using density-fitted CAM-B3LYP/STO-3G. The excited-state response was evaluated by the Tamm–Dancoff approximation in a frontier space containing the six highest occupied and six lowest virtual orbitals, with density-fitted Coulomb and seminumerical exchange response.

The three lowest rectangular-fragment roots occur at 2.0468, 2.4360, and 2.9513 eV, corresponding to 605.8, 509.0, and 420.1 nm, with oscillator strengths of 1.8765, 0.5229, and 0.3139. Their electron–hole centroid separations are 4.258, 3.946, and 5.301 Å. More than 99.1% of each displacement lies along the core-centroid connection axis. The final 5×5 to 6×6 active-space energy changes are below 0.0035 eV, and the assembled response matrix is Hermitian to approximately $10^{-7} E_{\mathrm{h}}$.

Relative to the ordinal DBC-fragment roots, the rectangular roots are 0.124–0.324 eV lower and have centroid separations 0.433–0.741 Å larger, although their oscillator strengths are smaller. Fragment populations show that the states remain predominantly bridge-centered; the results therefore establish directional excited-state polarization, not complete core-to-core charge separation. The calculation supports weak optical-directional admissibility while leaving charge-separation free energy, recombination competition, catalyst extraction, and hydrogen evolution unresolved. These distinctions motivate an uncertainty-aware inverse-design objective combining optical response, directional displacement, electron–hole overlap, redox alignment, kinetics, and synthetic feasibility.

Keywords: substituted chrysene; rectangular molecular networks; dibenzochrysene; directional excited-state polarization; charge displacement; range-separated density-functional theory; Tamm–Dancoff approximation; artificial photosynthesis; physics-informed inverse design.

1 Introduction and Unresolved Question

Visible-light absorption is necessary but not sufficient for artificial photosynthesis. Following photoexcitation, a material must produce an electronically useful redistribution of charge, suppress recombination, and deliver reducing equivalents to a catalytic interface. For Pt-assisted hydrogen evolution with a sacrificial electron donor, the intended sequence may be written schematically as

$$S_0 \xrightarrow{h\nu} X \xrightarrow{k_{\mathrm{CS}}} C \xrightarrow{k_{\mathrm{Pt}}} P, \qquad (1)$$

where S_0 is the electronic ground state, X is a photoexcited state, C is a charge-separated state, and P denotes a state in which the excess electron has been transferred toward a platinum acceptor. The existence of the first transition in Equation (1) does not imply the existence, energetic favorability, or kinetic competitiveness of either subsequent transition.

Dibenzochrysene-based covalent organic frameworks provide an experimental reference because a cyano-vinylene-connected DBC material has been reported to support visible-light hydrogen evolution under Pt-assisted, sacrificial-donor conditions

Citation: Schaper, C. D. (2026). Directional Excited-State Polarization in a 3,6,9,12-Connected Rectangular Chrysene Network: A Range-Separated Fragment Comparison with a Dibenzochrysene Benchmark. *Annals of the Chrysene Formalism*, 1(1), 459–475. https://chrysene.com/index.php/acf/article/view/38

[YHW+25]. That result establishes the experimental plausibility of a conjugated chrysene-related framework, but it does not establish that a distinct $3, 6, 9, 12$-connected substituted-chrysene architecture possesses the same excited-state properties. In particular, network connectivity and bridge orientation can alter transition energies, orbital amplitudes, spatial charge redistribution, and electronic coupling.

The proposed rectangular network is anisotropic. Its longer C12–C6 direction contains a cyano-vinylene bridge with $N + 2$ conjugated segments when the orthogonal C3–C9 direction contains N segments. The present study therefore examines the finite fragment

$$\mathfrak{R}_{2,y,f},$$

representing the longer direction for $N = 2$, and compares it with a finite DBC-derived node–bridge–node fragment

$$\mathfrak{K}_f.$$

Neither fragment is identified with its corresponding infinite, solvated, stacked, defect-containing, or catalyst-loaded material.

The immediate unresolved question is deliberately narrower than whether the rectangular material produces hydrogen. It is whether range-separated excited-state calculations identify at least one state satisfying

$$E_n > 0, \qquad f_n > 0, \qquad R_{\mathrm{eh},n} > 0, \qquad R_{\parallel,n} > 0, \tag{2}$$

where E_n is the excitation energy, f_n is the oscillator strength, $R_{\mathrm{eh},n}$ is the electron–hole centroid separation, and $R_{\parallel,n}$ is its magnitude along the node–bridge–node axis. Equation (2) defines a screening-level criterion for optically accessible directional charge displacement. It does not define a persistent or terminally localized charge-separated state.

The calculations reported below establish visible, optically allowed states in $\mathfrak{R}_{2,y,f}$ with electron–hole centroid separations of approximately 3.95–5.30 Å, more than 99.1% of which lies along the fragment axis. Fragment-resolved populations nevertheless remain predominantly bridge-centered. The result is therefore interpreted as directional excited-state polarization, not complete transfer of an electron from one chrysene core to the other.

Accordingly, the present work establishes only the first computational gate between absorption and useful photochemistry. The stronger conditions

$$\Delta G_{\mathrm{CS}} < 0, \qquad k_{\mathrm{CS}} > k_{\mathrm{rec}}, \qquad \Delta G_{\mathrm{Pt}} < 0, \qquad k_{\mathrm{Pt}} > 0 \tag{3}$$

remain unresolved, as do periodic transport, catalyst-mediated proton reduction, and measurable hydrogen evolution. The purpose of the finite fragment comparison is thus to determine whether the rectangular substituted-chrysene architecture is sufficiently plausible to justify those subsequent calculations and experiments.

2 Finite Fragments, Scope, and Admissibility Hierarchy

Definition 1 (Finite comparison fragments)**.** *Let*

$$\mathscr{F} = \left\{\mathfrak{K}_f, \mathfrak{R}_{2,y,f}\right\}.$$

The element $\mathfrak{K}_f$ is a finite DBC–cyano-vinylene–DBC node–bridge–node fragment derived from the connectivity of the experimentally studied kagome framework. The element $\mathfrak{R}_{2,y,f}$ is the finite fragment joining the C12 *site of one* $3, 6, 9, 12$*-substituted chrysene node to the* C6 *site of the adjacent node along the longer rectangular direction. For $N = 2$, this direction contains the prescribed $N + 2 = 4$ bridge segments.*

The molecular compositions used in the calculations are

$$\mathfrak{K}_f : \mathrm{C_{76}H_{44}N_2}, \qquad \mathfrak{R}_{2,y,f} : \mathrm{C_{78}H_{46}N_4}.$$

Thus, the comparison is protocol-matched but is not an atom-for-atom, mass-matched, or bridge-length-matched comparison. Its purpose is to determine whether the candidate fragment possesses the same class of screening-level optical and spatial observables as the DBC-derived reference, rather than whether the two fragments are chemically identical.

Hypothesis 1 (Matched-protocol convention)**.** *Every numerical comparison between $\mathfrak{K}_f$ and $\mathfrak{R}_{2,y,f}$ is made using the same exchange–correlation functional, one-electron basis, density-fitting convention, numerical integration grids, frontier-active response space, matrix-assembly procedure, and state-ordering rule.*

Hypothesis 1 controls methodological variation but does not remove chemical or geometric differences. Moreover, comparison of the n-th positive root of one fragment with the n-th positive root of the other is ordinal. It does not assert a one-to-one correspondence between diabatic electronic states.

Definition 2 (Admissibility hierarchy)**.** *For a candidate system X, define the following cumulative levels.*

A_0 Optical admissibility: *there exists an excited state n such that*

$$E_{n,X} > 0, \qquad f_{n,X} > 0.$$

A_1 Directional-polarization admissibility: A_0 *holds and*

$$R_{\mathrm{eh},n,X} > 0, \qquad R_{\parallel,n,X} > 0.$$

A_2 Charge-separation admissibility: A_1 *holds and an independently characterized charge-separated state* *satisfies*

$$\Delta G_{\mathrm{CS},X} < 0$$

together with a declared spatial-localization or electron–hole-overlap criterion.

A_3 Kinetic admissibility: A_2 *holds and*

$$k_{\mathrm{CS},X} > k_{\mathrm{rec},X} + k_{\mathrm{loss},X}.$$

A_4 Catalyst-extraction admissibility: A_3 *holds and, for at least one physically retained catalyst configuration,*

$$\Delta G_{\mathrm{Pt},X} < 0, \qquad V_{\mathrm{Pt},X} \neq 0, \qquad k_{\mathrm{Pt},X} > 0.$$

A_5 Experimental hydrogen-evolution admissibility: *illumination produces hydrogen above the analytical limit of quantification and above matched dark and no-material controls:*

$$R_{\mathrm{H}_2,X} > R_{\mathrm{LOQ}}.$$

Remark 1 (Logical scope of the present study)**.** *The calculations reported here evaluate only A_0 and A_1 for $\mathfrak{R}_{2,y,f}$, with $\mathfrak{K}_f$ serving as a finite-fragment reference. Levels A_2–A_5 are not inferred from directional centroid displacement. They require additional charged-state, environmental, kinetic, catalyst-interface, and experimental evidence.*

The present scope consequently excludes quantitative exciton binding, persistent charge separation, platinum injection, proton reduction, hydrogen-evolution rates, periodic transport, interlayer coupling, solvent response, sacrificial-donor chemistry, and metal-ion conditioning. It also excludes any inference that the finite DBC fragment reproduces the hydrogen-evolution activity of the corresponding periodic material. These exclusions preserve the intermediate result as a falsifiable statement about finite-fragment excited-state polarization rather than a claim of completed photocatalytic function.

2.1 Finite-fragment and partition conventions

The finite systems used in the present calculation are defined explicitly in Figure 1. Panel 1(a) establishes the chemical locant convention for the 3,6,9,12-substituted chrysene node. The two nominal lattice directions are the C3–C9 direction and the C12–C6 direction; only the latter is evaluated in the present study. Panel 1(b) records the coordinate constraints used during geometry conditioning. Panels 1(c) and 1(d) show the exact molecular graphs of the finite DBC benchmark fragment, $\mathfrak{K}_f$, and the rectangular C12–C6 fragment, $\mathfrak{R}_{2,y,f}$, respectively.

For each fragment, the heavy-atom set is partitioned as

$$\mathcal{V}_f = D \sqcup B \sqcup A,$$

where D is the left aromatic core, B is the intervening cyano-vinylene bridge, and A is the right aromatic core. This notation defines spatial regions for population and excited-state analysis. It does not assume, prior to calculation, that D and A are chemically distinct donor and acceptor moieties.

3 Computational Method Actually Performed

3.1 Fragment construction and geometry preparation

The molecular graphs of $\mathfrak{K}_f$ and $\mathfrak{R}_{2,y,f}$ were constructed from their prescribed aromatic nodes and cyano-vinylene bridges. Unused attachment valences were terminated with hydrogen. Initial extended, approximately planar coordinates were generated with RDKit. Because an unconstrained finite dimer can fold in a manner that is unavailable to a node embedded in an extended covalent network, the heavy-atom in-plane coordinates were treated as lattice constraints rather than freely optimized molecular coordinates.

The geometries used for the electronic-structure calculations were obtained with GFN2-xTB and an ALPB water environment [BEG19]. During this relaxation, the x- and y-coordinates of every heavy atom were fixed, whereas the out-of-plane coordinates and all hydrogen coordinates were allowed to relax. Optimization employed the FIRE algorithm with a maximum force criterion of

$$f_{\max} = 0.08\ \mathrm{eV}\,\text{Å}^{-1}.$$

No subsequent density-functional geometry optimization, vibrational analysis, conformational ensemble, or excited-state geometry optimization was performed.

3.2 Ground-state calculation

All electronic-structure calculations were carried out with PySCF 2.14.0 [SBB+18]. Each fragment was treated as a neutral, closed-shell singlet without spatial-symmetry constraints. The ground-state orbitals were calculated in the gas phase by restricted Kohn–Sham density-functional theory using the range-separated CAM-B3LYP functional [YTH04], the STO-3G orbital basis, and the Weigend auxiliary basis. Coulomb and exchange contributions to the ground-state calculation were evaluated with PySCF density fitting. A pruned level-zero numerical integration grid was used.

The self-consistent-field energy and gradient tolerances were

$$\tau_E = 10^{-7} E_{\mathrm{h}}, \qquad \tau_g = 3 \times 10^{-4},$$

with at most 160 SCF cycles. The DBC fragment was initialized from an atomic-density guess; the rectangular fragment was

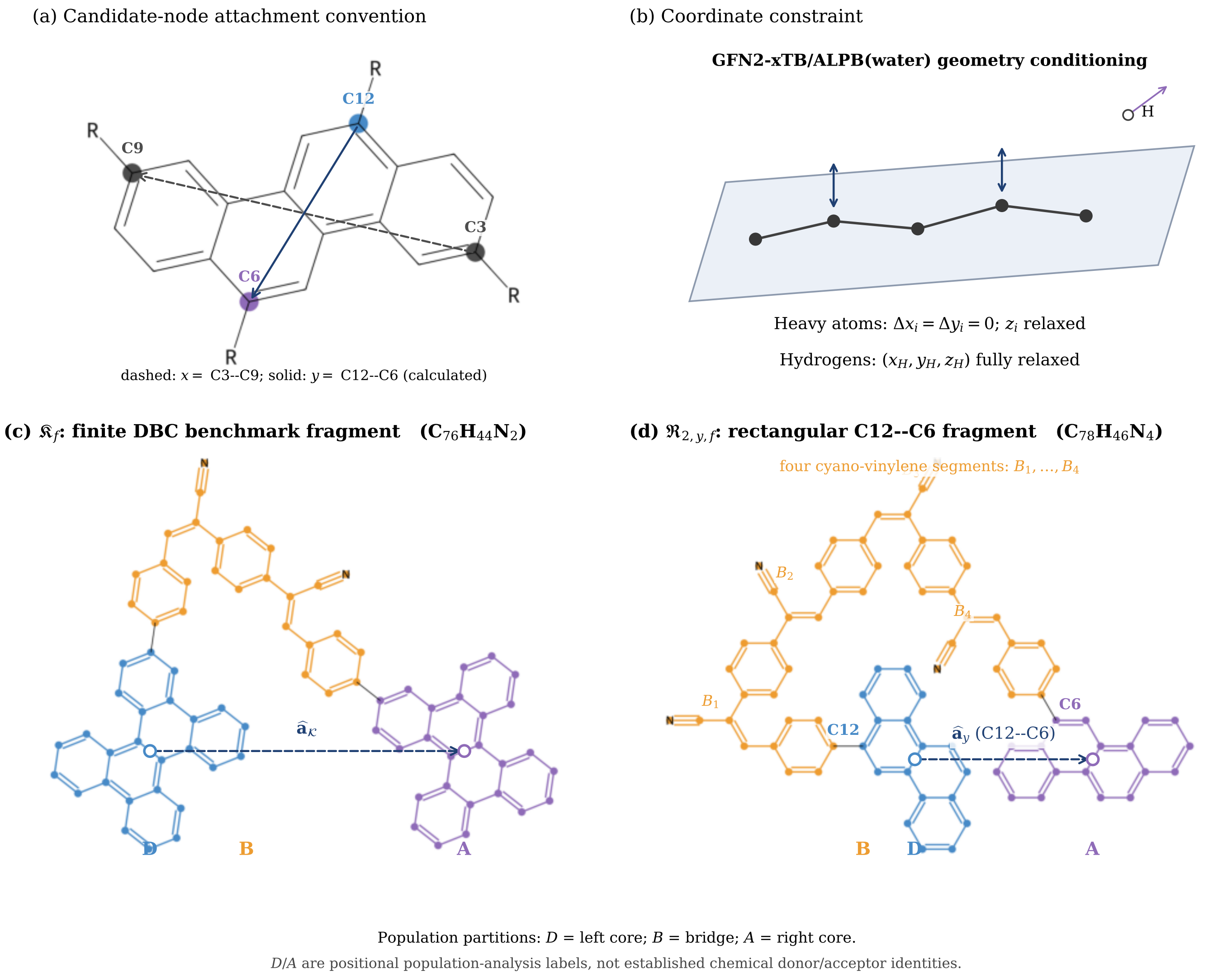

Figure 1: Finite-fragment, attachment-site, and population-partition conventions. **(a)** Locant convention for the 3,6,9,12-substituted chrysene node. The dashed direction joins C3 and C9, whereas the solid direction joins C12 and C6. The present excited-state calculation concerns the C12–C6 direction. **(b)** Geometry-conditioning convention. For each heavy atom i, the in-plane coordinates satisfy $\Delta x_i = \Delta y_i = 0$, while z_i is relaxed. Hydrogen coordinates are fully relaxed. Geometry conditioning employed GFN2-xTB with the ALPB water model; subsequent electronic-response calculations were performed as specified in the computational-method section. **(c)** Exact finite DBC benchmark fragment $\mathfrak{K}_f$. **(d)** Exact rectangular C12–C6 fragment $\mathfrak{R}_{2,y,f}$, containing the four cyano-vinylene segments $B_1, \ldots, B_4$. Blue, orange, and purple identify the positional D, B, and A population regions, respectively. The D/A notation does not imply an independently established chemical donor–acceptor pair.

initialized from a previously converged PBE/STO-3G density. The initial guesses were used only to accelerate convergence and do not alter the specified CAM-B3LYP equations. PySCF reported formal convergence for both fragments. The resulting total energies were

$$E_{\mathrm{SCF}}(\mathfrak{R}_f) = -2992.3128341173\, E_{\mathrm{h}},$$

and

$$E_{\mathrm{SCF}}(\mathfrak{R}_{2,y,f}) = -3176.3452649162\, E_{\mathrm{h}}.$$

The DBC post-convergence gradient norm was 5.96×10^{-5}. For the rectangular fragment, the final ordinary-cycle gradient norm was 2.02×10^{-4}, although the additional post-convergence cycle gave 6.28×10^{-4}. This discrepancy is retained as a numerical qualification rather than suppressed. The converged orbitals, occupations, orbital energies, density-fitting integrals, and SCF state were saved before constructing the excited-state response.

The specified SCF initial guess is a numerical initialization convention rather than a physical constraint on the final electronic state. Convergence therefore establishes a self-consistent stationary solution obtained from that initialization, but does not by itself prove uniqueness or convergence to the global variational minimum. A systematic comparison of alternative initial densities and orbital occupations remains part of the subsequent stability-validation gate.

3.3 Frontier-active TDA response

Definition 3 (Frontier-active response space)**.** *Let H and L denote the highest occupied and lowest unoccupied molecular orbitals, respectively. For $m \in \{2,3,4,5,6\}$, define*

$$\mathcal{V}_X^{(m)} = \operatorname{span}\{|i \to a\rangle : i \in \{H-m+1,\ldots,H\},\; a \in \{L,\ldots,L+m-1\}\}.$$

Thus,

$$\dim \mathcal{V}_X^{(m)} = m^2.$$

The reported calculation used $\mathcal{V}_X^{(6)}$, containing 36 *singly excited configurations.*

Singlet excitation energies were evaluated in the Tamm–Dancoff approximation [HHG99] using the saved CAM-B3LYP orbitals. Coulomb-response terms were treated by density fitting, whereas exchange-response terms were evaluated using level-one seminumerical exchange, denoted DF-J/SGX1-K.

For restartability, the 36×36 response matrix $A_X^{(6)}$ was evaluated as six separately checkpointed blocks, each containing six response columns. Following assembly, the departure from Hermiticity was measured by

$$\epsilon_\infty(X) = \max_{p,q} \left| (A_X^{(6)})_{pq} - (A_X^{(6)})^*_{qp} \right|,$$

and

$$\epsilon_{\mathrm{F}}(X) = \left\| A_X^{(6)} - A_X^{(6)\dagger} \right\|_{\mathrm{F}}.$$

The matrix used for diagonalization was its Hermitian part,

$$\widetilde{A}_X^{(6)} = \frac{1}{2}\left(A_X^{(6)} + A_X^{(6)\dagger} \right).$$

The three lowest positive eigenvalues exceeding $10^{-6} E_{\mathrm{h}}$ were retained.

For each root, the analysis produced the length-gauge oscillator strength, transition dipole, natural-transition-orbital weights, Löwdin attachment and detachment populations, electron and hole centroids, and the axial and transverse components of their displacement. Atomic populations were aggregated over the two aromatic cores and intervening bridge, denoted D, B, and A. Active-window sensitivity was estimated by diagonalizing the nested principal restrictions $\widetilde{A}_X^{(m)}$ for $m = 2,\ldots,6$.

Remark 2 (Computational status)**.** *The nested-window calculation tests only sensitivity within the constructed frontier hierarchy; it is not an independent full-orbital-space convergence study. The minimal orbital basis, fixed finite-fragment geometry, gas-phase response, SGX treatment, and ill-conditioned auxiliary Coulomb metric restrict all reported quantities to screening-level interpretation. No completed full-space TDA, solvent-response, charged-state, periodic, metal-containing, platinum-interface, or kinetic calculation is included in the results.*

4 Excited-State and Spatial Diagnostics

Let X_n denote the occupied–virtual TDA amplitude matrix associated with the n-th retained positive eigenvalue ω_n. The excitation energy and corresponding vacuum wavelength are

$$E_n = \hbar\omega_n, \qquad \lambda_n = \frac{hc}{E_n}. \tag{4}$$

Optical accessibility is characterized by the length-gauge oscillator strength f_n and transition-dipole vector $\boldsymbol{\mu}_n$.

Definition 4 (TDA hole and electron marginal matrices)**.** *Let C_{o} and C_{v} be the occupied and virtual molecular-orbital coefficient matrices. The unnormalized hole and electron marginal matrices in the atomic-orbital basis are*

$$D_{\mathrm{h},n} = C_{\mathrm{o}} X_n X_n^\dagger C_{\mathrm{o}}^\dagger, \tag{5}$$

$$D_{\mathrm{e},n} = C_{\mathrm{v}} X_n^\dagger X_n C_{\mathrm{v}}^\dagger. \tag{6}$$

Let S denote the atomic-orbital overlap matrix and define the Löwdin-transformed matrices

$$\widetilde{D}_{q,n} = S^{1/2} D_{q,n} S^{1/2}, \qquad q \in \{\mathrm{h},\mathrm{e}\}. \tag{7}$$

For atom a, let $\mathcal{I}(a)$ be the set of atomic-orbital indices centered on that atom. The normalized atomic weights used in the calculations are

$$w_{q,n}(a) = \frac{\sum_{\mu\in\mathcal{I}(a)} \max\{0, \mathrm{Re}(\widetilde{D}_{q,n})_{\mu\mu}\}}{\sum_{\nu} \max\{0, \mathrm{Re}(\widetilde{D}_{q,n})_{\nu\nu}\}}, \tag{8}$$

so that

$$w_{q,n}(a) \geq 0, \qquad \sum_a w_{q,n}(a) = 1.$$

Definition 5 (Electron–hole centroid displacement)**.** *Let $\mathbf{R}_a$ be the Cartesian coordinate of atom a. The hole and electron centroids are*

$$\mathbf{r}_{\mathrm{h},n} = \sum_a w_{\mathrm{h},n}(a)\mathbf{R}_a, \qquad \mathbf{r}_{\mathrm{e},n} = \sum_a w_{\mathrm{e},n}(a)\mathbf{R}_a. \tag{9}$$

Define

$$\Delta\mathbf{r}_n = \mathbf{r}_{\mathrm{e},n} - \mathbf{r}_{\mathrm{h},n}, \qquad R_{\mathrm{eh},n} = \|\Delta\mathbf{r}_n\|_2 . \tag{10}$$

For fragment X, let $\mathbf{c}_{D,X}$ and $\mathbf{c}_{A,X}$ be the unweighted heavy-atom centroids of its two aromatic cores. The oriented node–bridge–node axis is

$$\widehat{\mathbf{a}}_X = \frac{\mathbf{c}_{A,X} - \mathbf{c}_{D,X}}{\|\mathbf{c}_{A,X} - \mathbf{c}_{D,X}\|_2}. \tag{11}$$

Because interchange of the two core labels reverses this axis, the reported axial displacement is its absolute magnitude:

$$R_{\parallel,n,X} = \left|\Delta\mathbf{r}_{n,X} \cdot \widehat{\mathbf{a}}_X\right|, \tag{12}$$

$$R_{\perp,n,X} = \sqrt{R^2_{\mathrm{eh},n,X} - R^2_{\parallel,n,X}}, \tag{13}$$

$$\alpha_{\parallel,n,X} = \frac{R_{\parallel,n,X}}{R_{\mathrm{eh},n,X}}, \qquad R_{\mathrm{eh},n,X} > 0. \tag{14}$$

The corresponding transition-dipole axial fraction is

$$\eta_{\parallel,n,X} = \frac{|\boldsymbol{\mu}_{n,X} \cdot \widehat{\mathbf{a}}_X|}{\|\boldsymbol{\mu}_{n,X}\|_2}. \tag{15}$$

The quantities $\alpha_\parallel$ and $\eta_\parallel$ are distinct: the former describes the direction of electron–hole centroid displacement, whereas the latter describes optical-transition polarization.

Definition 6 (Fragment-resolved populations)**.** *Partition the atoms into the donor-side core D, bridge B, and acceptor-side core A. For $F \in \{D, B, A\}$, define*

$$h_{F,n} = \sum_{a\in F} w_{\mathrm{h},n}(a), \qquad e_{F,n} = \sum_{a\in F} w_{\mathrm{e},n}(a). \tag{16}$$

The core-to-bridge and opposite-core indices are

$$\chi_{\mathrm{CB},n} = (h_{D,n} + h_{A,n})e_{B,n}, \tag{17}$$

$$\chi_{\mathrm{opp},n} = \max\{h_{D,n}e_{A,n}, h_{A,n}e_{D,n}\}. \tag{18}$$

Finally, if

$$X_n = U_n\Sigma_n V_n^\dagger$$

is the singular-value decomposition of the transition-amplitude matrix, the normalized NTO weights are

$$p_{j,n} = \frac{\sigma^2_{j,n}}{\sum_k \sigma^2_{k,n}}, \qquad \sum_j p_{j,n} = 1. \tag{19}$$

The leading weight $p_{1,n}$ measures the extent to which one natural-transition-orbital pair represents the calculated excitation.

Remark 3 (Interpretive restriction)**.** *A large R_{eh} or $\alpha_\parallel$ does not, by itself, establish end-to-end charge separation. Two bridge-supported marginal distributions may possess different centroids while remaining localized predominantly on the same extended bridge. Directional polarization is therefore assigned only after joint examination of R_{eh}, $\alpha_\parallel$, $\eta_\parallel$, p_1, and the fragment populations.*

5 Results and Limited DBC Comparison

5.1 Ground-state and response-matrix diagnostics

Both closed-shell calculations reached formal SCF convergence. The ground-state energies were

$$E_{\mathrm{SCF}}(\mathfrak{R}_f) = -2992.3128341173\,E_\mathrm{h}, \tag{20}$$

$$E_{\mathrm{SCF}}(\mathfrak{R}_{2,y,f}) = -3176.3452649162\,E_\mathrm{h}. \tag{21}$$

The corresponding Kohn–Sham HOMO–LUMO gaps were approximately 2.747 and 2.587 eV, respectively. These orbital gaps are reported solely as SCF diagnostics; they are not identified with either fundamental or optical gaps.

Before Hermitian symmetrization, the maximum elementwise response-matrix asymmetries were

$$\epsilon_\infty(\mathfrak{R}_f) = 8.98 \times 10^{-8}\,E_\mathrm{h}, \tag{22}$$

$$\epsilon_\infty(\mathfrak{R}_{2,y,f}) = 1.14 \times 10^{-7}\,E_\mathrm{h}, \tag{23}$$

and the corresponding Frobenius norms were

$$\epsilon_\mathrm{F}(\mathfrak{R}_f) = 6.36 \times 10^{-7}\,E_\mathrm{h}, \qquad \epsilon_\mathrm{F}(\mathfrak{R}_{2,y,f}) = 6.12 \times 10^{-7}\,E_\mathrm{h}.$$

These deviations are several orders of magnitude smaller than the reported excitation energies. Hermitian symmetrization therefore introduces a negligible perturbation on the energy scale considered here, although it does not address basis-set or active-space error.

5.2 Optical energies and directional displacement

Table 1 gives the lowest three positive frontier-active TDA roots for both fragments. Each reported root has a strictly positive oscillator strength.

Proposition 1 (Visible directional roots)**.** *For each of the three calculated states of* $\mathfrak{R}_{2,y,f}$*,*

$$420 \text{ nm} < \lambda_n < 606 \text{ nm}, \qquad f_n > 0.31,$$

and

$$R_{\mathrm{eh},n} > 3.94\ \text{Å}, \qquad R_{\parallel,n} > 3.91\ \text{Å}, \qquad \alpha_{\parallel,n} > 0.991.$$

Consequently,

$$\mathsf{A}_1(\mathfrak{R}_{2,y,f}) = 1$$

within the finite-fragment and frontier-active model of Definition 2.

Proof. The smallest rectangular-fragment oscillator strength, centroid separation, axial displacement, and axial fraction in Table 1 are, respectively,

$$0.3139, \qquad 3.946\ \text{Å}, \qquad 3.911\ \text{Å}, \qquad 0.9911.$$

All three excitation energies are positive, and their wavelengths lie between 420.1 and 605.8 nm. The defining conditions of A_1 therefore hold. □

The transition-dipole axial fractions $\eta_\parallel$ for the three rectangular states were 0.9754, 0.8880, and 0.2975. Thus, S_1 and S_2 are predominantly polarized optically along the node–bridge–node axis. State S_3 has an almost completely axial electron–hole centroid displacement but a predominantly transverse transition dipole. This distinction confirms that optical-polarization direction and electron–hole displacement direction are independent observables.

The leading NTO weights range from 0.6283 to 0.9332 for the rectangular fragment. The lowest state is consequently well represented by one dominant NTO pair, whereas the higher states have greater multi-pair character. No state interpretation is based on the leading NTO alone.

5.3 Fragment-resolved character

The centroid results must be interpreted together with the fragment-resolved populations in Table 2. For every state, the hole and electron populations sum separately to unity up to rounding.

Proposition 2 (Bridge-dominated rectangular states)**.** *For every reported state of* $\mathfrak{R}_{2,y,f}$*,*

$$h_{B,n} > 0.62, \qquad e_{B,n} > 0.74, \qquad \chi_{\mathrm{opp},n} < 0.014.$$

The calculated states therefore cannot be identified with complete transfer from one chrysene core to the opposite chrysene core.

Proof. From Table 2,

$$\min_n h_{B,n} = 0.6282,$$
$$\min_n e_{B,n} = 0.7411,$$
$$\max_n \chi_{\mathrm{opp},n} = 0.0136.$$

These values imply that both marginal distributions have their largest population on the bridge, whereas simultaneous opposite-core hole and electron localization remains small. □

Proposition 2 does not contradict Proposition 1. Two distributions may both occupy an extended bridge while having distinct centroids. The combined result is therefore directional redistribution within the node–bridge–node fragment, dominated by polarization along the bridge.

5.4 Frontier-window sensitivity

The final enlargement of the active space was assessed through the difference

$$\delta^{(5\to6)}_{n,X} = \left| E^{(6)}_{n,X} - E^{(5)}_{n,X} \right|.$$

The resulting increments are listed in Table 3.

For $\mathfrak{R}_{2,y,f}$,

$$\max_{1\le n\le 3} \delta^{(5\to6)}_{n,\mathfrak{R}} = 0.0034 \text{ eV}.$$

The rectangular roots are therefore stable under the final tested frontier-window enlargement. This result is internal to the nested principal-submatrix hierarchy and does not imply convergence with respect to the complete occupied–virtual space, orbital basis, geometry, dielectric environment, or response approximation. The larger S_2 increment of the DBC fragment, 0.0976 eV, indicates greater active-window sensitivity for that ordinal root.

5.5 Limited ordinal comparison with the DBC fragment

Because root order does not establish electronic-state identity across chemically different fragments, define only the ordinal differences

$$\Delta E_j = E_{j,\mathfrak{R}} - E_{j,\mathfrak{K}}, \qquad \Delta R_j = R_{\mathrm{eh},j,\mathfrak{R}} - R_{\mathrm{eh},j,\mathfrak{K}}. \tag{24}$$

Table 1: Lowest three frontier-active CAM-B3LYP/TDA roots. Here E_n is the excitation energy, λ_n is the corresponding vacuum wavelength, f_n is the length-gauge oscillator strength, R_{eh} is the electron–hole centroid separation, $R_\parallel$ is its absolute axial component, $\alpha_\parallel = R_\parallel / R_{\text{eh}}$, and p_1 is the leading NTO weight.

System	State	E_n (eV)	λ_n (nm)	f_n	R_{eh} (Å)	$R_\parallel$ (Å)	$\alpha_\parallel$	p_1
$\mathfrak{K}_f$	S_1	2.3712	522.9	2.4716	3.778	3.753	0.9932	0.9327
	S_2	2.5601	484.3	0.8474	3.206	3.147	0.9818	0.7318
	S_3	3.1156	397.9	0.6794	4.868	2.073	0.4259	0.7355
$\mathfrak{R}_{2,y,f}$	S_1	2.0468	605.8	1.8765	4.258	4.255	0.9992	0.9332
	S_2	2.4360	509.0	0.5229	3.946	3.911	0.9911	0.6885
	S_3	2.9513	420.1	0.3139	5.301	5.300	0.9997	0.6283

Table 2: Löwdin hole and electron populations on the donor-side core D, bridge B, and acceptor-side core A. The indices are $\chi_{\text{CB}} = (h_D + h_A)e_B$ and $\chi_{\text{opp}} = \max\{h_D e_A, h_A e_D\}$.

System	State	h_D	h_B	h_A	e_D	e_B	e_A	χ_{CB}	χ_{opp}
$\mathfrak{K}_f$	S_1	0.2316	0.7282	0.0402	0.0839	0.8268	0.0893	0.2247	0.0207
	S_2	0.0655	0.8284	0.1061	0.1967	0.7895	0.0138	0.1355	0.0209
	S_3	0.6467	0.2687	0.0847	0.1991	0.7662	0.0347	0.5604	0.0224
$\mathfrak{R}_{2,y,f}$	S_1	0.0046	0.7702	0.2252	0.0050	0.9167	0.0783	0.2106	0.0011
	S_2	0.0138	0.9186	0.0676	0.0013	0.7411	0.2576	0.0604	0.0036
	S_3	0.0197	0.6282	0.3521	0.0386	0.8196	0.1418	0.3047	0.0136

Table 3: Absolute changes in the three lowest roots under the final $5o/5v$ to $6o/6v$ frontier-window enlargement.

System	δ_1 (eV)	δ_2 (eV)	δ_3 (eV)
$\mathfrak{K}_f$	0.0180	0.0976	0.0180
$\mathfrak{R}_{2,y,f}$	0.0034	0.0028	0.0023

The computed values are

$$(\Delta E_1, \Delta E_2, \Delta E_3) = (-0.3244, -0.1240, -0.1644)\ \text{eV},$$

and

$$(\Delta R_1, \Delta R_2, \Delta R_3) = (0.480, 0.741, 0.433)\ \text{Å}.$$

Hence, for every $j \in \{1, 2, 3\}$,

$$E_{j,\mathfrak{R}} < E_{j,\mathfrak{K}}, \qquad R_{\text{eh},j,\mathfrak{R}} > R_{\text{eh},j,\mathfrak{K}}, \qquad f_{j,\mathfrak{R}} > 0.$$

Conversely, the DBC oscillator strengths exceed the corresponding rectangular values for all three ordinal roots. Neither fragment therefore dominates the other over the joint observable vector

$$\left(E,\ f,\ R_{\text{eh}},\ \alpha_\parallel,\ p_1,\ \chi_{\text{opp}}\right).$$

Theorem 3 (Limited finite-fragment conclusion). *Under the matched CAM-B3LYP/TDA screening protocol, $\mathfrak{R}_{2,y,f}$ is not excluded relative to $\mathfrak{K}_f$ with respect to the existence of visible, optically allowed states having nonzero directional electron–hole displacement. This conclusion does not imply relative photocatalytic performance, persistent charge separation, favorable catalyst extraction, or hydrogen evolution.*

Proof. The optical and spatial claim follows from Proposition 1 and the ordinal inequalities above. Proposition 2 shows that the same states are predominantly bridge-centered and therefore do not establish terminal core-to-core separation. No charge-separation free energy, competing rate constant, platinum-interface quantity, or hydrogen-evolution rate was calculated. The stronger conclusions consequently do not follow from the reported data. □

6 Uncertainty, Sensitivity, and Falsifiability

The numerical values in Section 5 are deterministic outputs of the specified finite-fragment model. Their reproducibility within that model must be distinguished from their robustness under changes in basis, geometry, electronic-structure approximation, and physical environment.

6.1 Numerical and active-space sensitivity

Three internal numerical checks were available. First, the maximum pre-symmetrization response-matrix errors were

$$\epsilon_\infty(\mathfrak{K}_f) = 8.98 \times 10^{-8}\, E_{\text{h}}, \qquad \epsilon_\infty(\mathfrak{R}_{2,y,f}) = 1.14 \times 10^{-7}\, E_{\text{h}}.$$

These values are negligible relative to the 2–3 eV excitation-energy scale. The reported roots are therefore insensitive to the explicit Hermitian projection at the displayed precision.

Second, the largest rectangular-fragment energy change under the final $5o/5v$ to $6o/6v$ enlargement was

$$\max_{1\le n\le 3} \delta^{(5\to 6)}_{n,\mathfrak{R}} = 0.0034 \text{ eV}.$$

The corresponding DBC maximum was 0.0976 eV, arising from its second ordinal root. Thus, the rectangular roots are internally stable at the upper end of the tested frontier hierarchy, whereas at least one DBC root remains more sensitive to the frontier-space boundary. Neither result establishes convergence in the full occupied–virtual space.

Third, PySCF reported formal SCF convergence for both fragments. For $\mathfrak{R}_{2,y,f}$, however, the final ordinary-cycle gradient norm was

$$2.02\times 10^{-4},$$

whereas the additional post-convergence cycle produced

$$6.28\times 10^{-4},$$

which exceeds the requested threshold 3.0×10^{-4}. The corresponding energy change was only $9.59\times 10^{-8} E_\mathrm{h}$. This behavior suggests local gradient sensitivity associated with the coarse integration grid or density-fitting representation and is retained as an explicit qualification.

The Weigend auxiliary Coulomb metrics also had small estimated reciprocal condition numbers,

$$\kappa_{\mathfrak{K}}^{-1} \approx 3.54\times 10^{-20}, \qquad \kappa_{\mathfrak{R}}^{-1} \approx 1.62\times 10^{-20}.$$

Although the assembled response matrices were nearly Hermitian, these values indicate severe linear dependence in the auxiliary representation. Confirmation with a better-conditioned auxiliary basis is therefore required before assigning quantitative spectroscopic accuracy.

Proposition 4 (Status of internal stability)**.** *The rectangular-fragment roots are internally stable with respect to response-matrix assembly and the final tested active-window enlargement. They have not been shown to be model-robust with respect to the orbital basis, auxiliary basis, geometry, dielectric environment, or complete response space.*

Proof. Internal stability follows from the response-matrix errors below $1.2\times 10^{-7} E_\mathrm{h}$ and the final-window energy changes below 0.0035 eV. Model robustness would require the same qualitative states and directional observables to persist over independent changes in basis, geometry, environment, and response space. Those calculations were not performed, so the stronger conclusion does not follow. □

6.2 Uncertainty hierarchy

The principal unquantified uncertainties are:

1. *basis uncertainty*, because STO-3G lacks sufficient polarization and diffuse flexibility for quantitative excited-state or charge-displacement analysis;
2. *active-space uncertainty*, because only the six highest occupied and six lowest virtual orbitals were retained;
3. *structural uncertainty*, because one constrained GFN2-xTB geometry was used for each fragment without a conformer, torsional, defect, or thermal ensemble;
4. *environmental uncertainty*, because the electronic response was evaluated in the gas phase without dielectric, solvent, counterion, or sacrificial-donor effects;
5. *finite-size uncertainty*, because a hydrogen-capped node–bridge–node fragment does not represent periodic delocalization, interlayer stacking, disorder, or surface termination; and
6. *mechanistic uncertainty*, because charged states, recombination, catalyst extraction, and proton reduction were not calculated.

Definition 7 (Prospective model-ensemble interval)**.** *Let $\mathcal{M}$ be a prospectively declared ensemble of admissible basis sets, geometries, response spaces, and environments. For any scalar diagnostic Q, define*

$$I_Q(\mathcal{M}) = \left[\min_{\mu\in\mathcal{M}} Q_\mu,\ \max_{\mu\in\mathcal{M}} Q_\mu\right].$$

A threshold-dependent claim $Q \ge Q_{\min}$ is called robust over $\mathcal{M}$ only if

$$\inf I_Q(\mathcal{M}) \ge Q_{\min}.$$

For subsequent calculations, reasonable prospective screening thresholds are

$$400 \text{ nm} \le \lambda \le 700 \text{ nm}, \qquad f \ge 10^{-2},$$

and

$$R_\parallel \ge 2.0 \text{ Å}, \qquad \alpha_\parallel \ge 0.80.$$

These thresholds were not preregistered before the present calculation and are not used to prove Theorem 3. Their purpose is to make the next model-refinement stage prospectively falsifiable.

6.3 Falsifiability sequence

The model-internal result can be checked by independent reimplementation of the saved geometries, SCF checkpoints, response

Table 4: Prospective tests distinguishing computational reproducibility from physical admissibility. Failure at a later gate does not erase the model-internal calculation, but it prevents the corresponding stronger interpretation.

Gate	Required confirmation	Falsifying or disqualifying outcome
Implementation	Independent reconstruction reproduces the assembled active-space matrix, roots, oscillator strengths, and centroid diagnostics within declared numerical tolerances.	Material disagreement traceable to indexing, fragment assignment, matrix assembly, normalization, or unit conversion.
Electronic-structure refinement	Visible, allowed, axially displaced states persist with a polarized basis, a stable auxiliary basis, and an enlarged response space.	No state satisfying the prospective optical and axial thresholds survives state tracking across the refined calculations.
Geometry and environment	Directional displacement persists over retained torsional geometries and physically relevant dielectric or solvent conditions.	The qualifying states disappear, become dark, or lose directional displacement throughout the admissible geometry–environment ensemble.
Strong charge-separation gate	A spatially characterized state satisfies $\Delta G_{\mathrm{CS}} < 0$ and forms competitively with recombination and nonradiative loss.	All physically admissible models give $\Delta G_{\mathrm{CS}} \geq 0$, negligible electronic coupling, or $k_{\mathrm{CS}} \leq k_{\mathrm{rec}} + k_{\mathrm{loss}}$.
Catalyst and experiment	Electron transfer to a retained catalyst configuration is favorable, and illuminated samples exceed dark, no-material, and no-catalyst controls.	No favorable extraction channel is found, or hydrogen remains at or below the analytical limit and matched controls.

blocks, and diagnostic equations. The broader physical hypothesis requires progressively stronger tests, summarized in Table 4.

The limited DBC comparison has an additional uncertainty: the two fragments differ in molecular composition, bridge length, node identity, and state character. Ordinal inequalities in E_n and $R_{\mathrm{eh},n}$ must therefore not be interpreted as calibrated errors relative to experiment or as evidence of superior photocatalytic performance. The comparison establishes only that the rectangular fragment possesses a nonzero, visible, directional excited-state response under the same screening protocol.

Accordingly, the present result is both positive and falsifiable. It supports continued calculation because the candidate does more than absorb light within the reduced model. It remains provisional because the persistence of that polarization, its conversion into a long-lived charge-separated state, and its delivery to a catalyst have not yet been demonstrated.

7 Implications for Inverse Design

The present calculation does not identify a completed photocatalyst. It identifies which observables must be included in an inverse-design system intended to progress from light absorption toward useful charge separation. In particular, the simultaneous existence of visible absorption and a nonzero electron–hole centroid displacement does not determine where the corresponding marginal distributions reside.

Proposition 5 (Insufficiency of an absorption–centroid objective)**.** *Within the present finite-fragment model, the conditions*

$$400 \text{ nm} < \lambda_n < 700 \text{ nm}, \qquad f_n > 0, \qquad R_{\mathrm{eh},n} > 0$$

do not imply substantial opposite-core charge separation.

Proof. All three states of $\mathfrak{R}_{2,y,f}$ satisfy the stated optical and centroid conditions. Nevertheless, Proposition 2 gives

$$h_{B,n} > 0.62, \qquad e_{B,n} > 0.74, \qquad \chi_{\mathrm{opp},n} < 0.014.$$

Thus, both marginal distributions remain predominantly bridge-centered while the opposite-core transfer index remains small. The asserted implication is therefore false. □

Proposition 5 does not make bridge-centered polarization undesirable. An extended bridge may serve as a transport pathway or place electron density near a catalyst-binding site. It does require that the desired localization pattern be specified explicitly. A design intended to produce core-to-core separation should reward terminal localization, whereas a design intended for catalyst extraction should reward electron population at the designated catalyst-facing region.

7.1 Design variables and forward observables

Let Θ be the chemically admissible design space. A candidate $\theta \in \Theta$ may be represented by

$$\theta = \left(G_{\mathrm{node}}, \mathbf{s}, N_x, N_y, \boldsymbol{\phi}, d_{\mathrm{stack}}, \mathbf{u}_{\mathrm{slip}}, \psi_{\mathrm{twist}}, \mathcal{E}\right), \qquad (25)$$

where G_{node} specifies the molecular graph, $\mathbf{s}$ specifies the substituents at the available attachment sites, N_x and N_y specify the two bridge lengths, $\boldsymbol{\phi}$ contains bridge and node torsions,

d_{stack}, $\mathbf{u}_{\text{slip}}$, and ψ_{twist} specify interlayer geometry, and $\mathcal{E}$ denotes the dielectric and chemical environment. For the rectangular recurrence considered here,

$$N_y = N_x + 2, \qquad N_x \in 2\mathbb{N}_0.$$

The corresponding forward-property map is not scalar. At a minimum, it must return

$$\mathcal{F}(\theta) = \left(E_{\text{opt}}, f, R_\parallel, \alpha_\parallel, \eta_\parallel, p_1, \mathbf{h}, \mathbf{e}, \chi_{\text{opp}}, S_{\text{eh}}, \Delta G_{\text{CS}}, \Gamma_{\text{CS}}, \Delta G_{\text{Pt}}\right), \tag{26}$$

where

$$\mathbf{h} = (h_D, h_B, h_A), \qquad \mathbf{e} = (e_D, e_B, e_A),$$

and S_{eh} is a prospective electron–hole overlap diagnostic. One population-based choice is

$$S_{\text{eh}} = \sum_a \sqrt{w_{\text{h}}(a) w_{\text{e}}(a)}, \qquad 0 \le S_{\text{eh}} \le 1. \tag{27}$$

The kinetic competition number may subsequently be defined as

$$\Gamma_{\text{CS}} = \frac{k_{\text{CS}}}{k_{\text{rec}} + k_{\text{loss}}}.$$

Only the optical and spatial components of Equation (26) were evaluated in the present study.

7.2 Hierarchical feasible sets

The inverse problem should be solved through nested feasibility gates rather than by maximizing one optical score. Define

$$\Theta_0 = \{\theta \in \Theta : \theta \text{ is chemically valid and structurally realizable}\}, \tag{28}$$

$$\Theta_1 = \left\{\theta \in \Theta_0 : E_{\text{opt}} \in I_{\text{vis}},\ f \ge f_{\min}\right\}, \tag{29}$$

$$\Theta_2 = \left\{\theta \in \Theta_1 : R_\parallel \ge R_{\min},\ \alpha_\parallel \ge \alpha_{\min}\right\}, \tag{30}$$

$$\Theta_3 = \left\{\theta \in \Theta_2 : \begin{array}{l} \mathcal{L}(\mathbf{h}, \mathbf{e}, S_{\text{eh}}) \\ \text{satisfies the prescribed localization mechanism} \end{array}\right\}, \tag{31}$$

$$\Theta_4 = \{\theta \in \Theta_3 : \Delta G_{\text{CS}} < 0,\ \Gamma_{\text{CS}} > 1\}, \tag{32}$$

$$\Theta_5 = \{\theta \in \Theta_4 : \Delta G_{\text{Pt}} < 0,\ V_{\text{Pt}} \ne 0\}. \tag{33}$$

Here I_{vis} is the target spectral interval, and $\mathcal{L}$ is a mechanism-specific localization functional. The present calculation provides evidence that

$$\Theta_2 \ne \varnothing$$

within the reduced fragment model. It provides no conclusion about the nonemptiness of Θ_3, Θ_4, or Θ_5.

7.3 Anisotropic and uncertainty-aware ranking

Because the rectangular architecture is direction-dependent, its forward model should preserve directional quantities:

$$\mathcal{F}_{\text{dir}}(\theta) = \left(R_{\parallel,x}, R_{\parallel,y}, T_x, T_y, D_{xx}, D_{yy}\right).$$

No constraint of the form

$$R_{\parallel,x} = R_{\parallel,y} \quad \text{or} \quad D_{xx} = D_{yy}$$

is required. A useful architecture may absorb or redistribute charge preferentially along one direction while using the orthogonal direction for structural connectivity, transport, or catalyst placement. The present y-fragment result therefore motivates directional objectives, but it does not establish a two-dimensional transport tensor; the x-direction and periodic network remain separate calculations.

Let a forward predictor return a mean $\mu_j(\theta)$ and calibrated uncertainty $\sigma_j(\theta)$ for each property Q_j. A conservative benefit score and risk score may be defined by

$$Q_j^{\text{LCB}}(\theta) = \mu_j(\theta) - \beta_j \sigma_j(\theta), \qquad Q_j^{\text{UCB}}(\theta) = \mu_j(\theta) + \beta_j \sigma_j(\theta), \tag{34}$$

with $\beta_j > 0$ fixed before candidate ranking. Beneficial quantities are ranked by lower confidence bounds, whereas penalties such as overlap, strain, or recombination are ranked by upper confidence bounds. Candidates should be retained on an uncertainty-qualified Pareto front rather than collapsed immediately to one weighted scalar score.

Theorem 6 (Inverse-design consequence of the fragment calculation)**.** *Any inverse-design workflow for the rectangular chrysene system that optimizes only excitation energy and oscillator strength is insufficient to distinguish absorption from directional polarization or terminal charge separation. A minimally admissible workflow must additionally include at least one directional displacement observable and one localization or overlap observable.*

Proof. Proposition 5 shows that visible, optically allowed states with nonzero centroid displacement may remain predominantly bridge-centered. Excitation energy and oscillator strength therefore do not determine the spatial distribution of the hole and electron. Directional displacement and localization information are logically independent inputs to candidate classification. □

The quantum-chemical results obtained here may consequently serve as initial labels and calibration cases for a future forward predictor, including a three-dimensional equivariant graph neural network. Constrained generation would propose chemically valid structures; the forward model would predict the vector in Equation (26); uncertainty-aware ranking would select candidates for higher-level TD-DFT, charged-state, periodic, and catalyst-interface calculations; and experimental measurements would update the predictor. The role of the present calculation is to prevent that loop from treating absorption alone as evidence of photosynthetic function.

8 Limitations and Next Computational Gates

The present calculation is intentionally restricted to a finite, fixed-geometry, gas-phase, frontier-active model. Its principal limitations arise from the STO-3G orbital basis, the ill-conditioned auxiliary Coulomb metric, the $6o/6v$ response space, the SGX exchange response, and the use of one constrained GFN2-xTB geometry for each fragment. The calculation contains no explicit dielectric environment, structural ensemble, charged state, periodic lattice, interlayer stack, metal ion, sacrificial donor, or catalyst interface.

The DBC comparison is likewise limited. The finite fragments differ in composition, bridge length, and node identity, and the comparison between their j-th roots is ordinal rather than diabatic. Consequently, the results neither reproduce the experimentally reported DBC hydrogen-evolution rate nor establish relative photocatalytic performance.

> **Definition 8** (Computational gate)**.** *A computational gate is a prospectively specified calculation together with an acceptance criterion. Gate G_{j+1} may support a stronger physical interpretation only after gate G_j has been completed without a disqualifying result.*

The following sequence separates refinement of the present result from the stronger thermodynamic, kinetic, and catalyst-level questions.

G_1 Basis and response-space confirmation. Repeat the lowest relevant roots using a polarized split-valence basis, a compatible well-conditioned auxiliary basis, a finer integration grid, and progressively enlarged occupied–virtual spaces. States shall be tracked by NTO overlap, fragment populations, and transition-density character, rather than root number alone. Gate G_1 is passed only if at least one state retains

$$\lambda \in I_{\mathrm{vis}}, \qquad f \geq f_{\min}, \qquad R_{\parallel} \geq R_{\min}, \qquad \alpha_{\parallel} \geq \alpha_{\min}.$$

G_2 Structural and environmental persistence. Recalculate the qualifying states over a declared ensemble of bridge torsions, constrained lattice geometries, and dielectric environments. The ensemble should include solvent-conditioned and low-polarity limits. Gate G_2 requires the uncertainty-qualified intervals

$$\inf I_f > 0, \qquad \inf I_{R_{\parallel}} > 0,$$

together with persistent directional and localization character. Loss of the state throughout the admissible ensemble falsifies its proposed physical relevance.

G_3 Exciton and charge-separation energetics. Calculate consistent vertical ionization potentials and electron affinities using a range-separated method with polarization and diffuse flexibility. Determine

$$E_{\mathrm{fund}} = I_{\mathrm{v}} - A_{\mathrm{v}}, \qquad E_b^{\mathrm{eff}} = E_{\mathrm{fund}} - E_{\mathrm{opt}}.$$

A donor–acceptor or bridge–acceptor partition shall then be evaluated by constrained or fragment-based charged-state calculations to determine

$$\Delta G_{\mathrm{CS}} = G_C - G_X.$$

Gate G_3 requires a spatially characterized state for which the uncertainty interval of ΔG_{CS} includes a physically relevant favorable domain.

G_4 Separation–recombination competition. Determine the diabatic couplings, reorganization energies, and free-energy changes required to estimate k_{CS} and k_{rec} under the same environmental convention. The relevant decision variable is

$$\Gamma_{\mathrm{CS}} = \frac{k_{\mathrm{CS}}}{k_{\mathrm{rec}} + k_{\mathrm{loss}}}.$$

A strong kinetic result requires $\Gamma_{\mathrm{CS}} > 1$ over a nonempty, physically admissible parameter domain.

G_5 Catalyst-directed electron extraction. Introduce a defined catalyst-facing site and evaluate first its redox alignment and electronic coupling, followed by explicit retained Pt-cluster configurations. For at least one stable interface, determine

$$\Delta G_{\mathrm{Pt}}, \qquad V_{\mathrm{Pt}}, \qquad k_{\mathrm{Pt}}.$$

Gate G_5 requires a nonzero extraction channel and favorable competition between extraction and recombination. It does not by itself establish proton reduction.

G_6 Oligomeric, periodic, and metal-conditioned extension. Extend the validated fragment calculation first along the C12–C6 direction and then to the two-dimensional rectangular and stacked systems. A bounded metal-conditioned branch may subsequently evaluate selected metal identities, oxidation and spin states, metal–π distances, counterions, and coordination environments. Such conditioning is treated as a controlled design variable, not as evidence that an unfavorable metal-free mechanism has been repaired.

> **Remark 4** (Experimental boundary)**.** *Completion of G_1–G_6 would justify prospective optical, electrochemical, time-resolved, and Pt-assisted hydrogen-evolution measurements.*

> *No computational gate substitutes for comparison against illuminated, dark, no-material, and no-catalyst controls.*

This sequence preserves the present result at its proper logical level: it establishes a reproducible candidate state for further study, while making every stronger inference contingent upon a specific calculation or experiment capable of rejecting it.

9 Conclusion

This work examined whether the longer C12–C6 direction of a 3, 6, 9, 12-connected rectangular substituted-chrysene network supports an electronically meaningful response beyond light absorption. A finite rectangular node–bridge–node fragment, $\mathfrak{R}_{2,y,f}$, was compared with a finite DBC-derived fragment, $\mathfrak{K}_f$, using the same frontier-active CAM-B3LYP/TDA screening protocol.

For $\mathfrak{R}_{2,y,f}$, the three lowest calculated roots occurred at

$$2.0468, \qquad 2.4360, \qquad 2.9513 \text{ eV},$$

corresponding to

$$605.8, \qquad 509.0, \qquad 420.1 \text{ nm}.$$

All three states were optically allowed, with oscillator strengths of 1.8765, 0.5229, and 0.3139. Their electron–hole centroid separations were

$$4.258, \qquad 3.946, \qquad 5.301 \text{ Å},$$

and more than 99.1% of each displacement lay along the node–bridge–node axis. The corresponding roots changed by less than 0.0035 eV under the final $5o/5v$ to $6o/6v$ frontier-window enlargement.

Furthermore, the Weigend auxiliary Coulomb metrics exhibited severe linear dependence, with estimated reciprocal condition numbers of approximately 1.62×10^{-20} and 3.54×10^{-20}. Confirmation with a better-conditioned auxiliary basis (Gate G_1) is therefore strictly required before assigning quantitative spectroscopic accuracy to these states.

Relative to the ordinal DBC-fragment roots, the rectangular roots were 0.124–0.324 eV lower and their centroid separations were 0.433–0.741 Å larger. This comparison establishes neither chemical equivalence nor photocatalytic superiority. It shows only that the rectangular fragment is not excluded, relative to the finite DBC reference, from possessing visible and directionally displaced excited states within the matched reduced model.

Fragment-resolved populations impose the decisive qualification: for the rectangular states,

$$h_B > 0.62, \qquad e_B > 0.74, \qquad \chi_{\text{opp}} < 0.014.$$

The calculated response is therefore most accurately described as directional excited-state polarization along the extended bridge, not complete transfer of an electron from one chrysene core to the opposite core. Consequently,

$$\mathsf{A}_1(\mathfrak{R}_{2,y,f}) = 1,$$

whereas the stronger admissibility levels A_2–A_5 remain unresolved.

The principal inverse-design implication is that excitation energy and oscillator strength are insufficient objectives. A defensible workflow must also represent directional displacement, electron–hole overlap, fragment localization, charge-separation free energy, recombination competition, catalyst extraction, structural feasibility, and uncertainty. The present calculation supplies an intermediate but falsifiable result: the rectangular chrysene architecture is electronically plausible enough to justify higher-level basis, environmental, charged-state, kinetic, periodic, and catalyst-interface calculations, but persistent charge separation and hydrogen evolution remain open experimental propositions.

A Literature Context and Relation to the Present Calculation

A.1 Conjugated organic frameworks for photocatalytic hydrogen evolution

Covalent organic frameworks (COFs) provide the closest established materials context for the present investigation. Their periodic covalent structures permit optical absorption, exciton migration, charge transport, pore formation, and catalyst loading to be modified through the selection of the aromatic node and conjugated bridge. Nevertheless, visible-light absorption alone is not sufficient to establish photocatalytic activity: productive hydrogen evolution additionally requires charge separation, electron delivery to a reduction site, suppression of recombination, and appropriate interfacial chemistry.

Early azine-linked COFs demonstrated that the photocatalytic response could be systematically varied through the electronic composition of the framework [VHS+15]. Diacetylene-containing frameworks subsequently showed that changing the conjugated bridge can materially alter the hydrogen-evolution response, even when the overall framework design remains similar [PAR+18]. Sulfone-containing COFs further demonstrated that photocatalytic performance depends jointly on electronic structure, crystallinity, visible-light absorption, pore accessibility, and interaction with the reaction medium [WCC+18]. These studies establish that neither topology nor optical absorption should be interpreted independently of bridge chemistry and solid-state organization.

Particularly relevant to the present paper is the donor–acceptor framework studied by Li *et al.* [LLL+22]. In that system, donor–acceptor organization was associated with reduced exciton binding, longer-lived charge carriers, and enhanced Pt-assisted sacrificial hydrogen evolution. The result supports the general design proposition

$$\text{spatially differentiated excitation} \implies \text{potentially improved charge separation},$$

but it does not make the implication unconditional. The energetic ordering, electronic coupling, dielectric environment, and competing decay rates must also be favorable.

Most of these experiments employ a sacrificial electron donor and a deposited metal cocatalyst. They therefore test the reduction side of a photocatalytic cycle rather than unbiased overall water splitting. In logical terms,

$$R_{\mathrm{H}_2}^{\mathrm{sac,Pt}} > 0 \quad \not\Rightarrow \quad R_{\mathrm{H}_2}^{\mathrm{overall}} > 0.$$

This distinction motivates the restricted admissibility hierarchy used in the present work.

A.2 Dibenzochrysene as the experimental benchmark

The electronic properties of dibenzo[g,p]chrysene derivatives are sensitive to substitution pattern, torsion, and frontier-orbital distribution [IAY+22]. This sensitivity makes dibenzochrysene a useful reference for determining how an extended aromatic node interacts with conjugated attachments.

The immediate experimental benchmark is the dibenzo[g,p]chrysene-based, sp^2 carbon-linked kagome COF reported by Yu *et al.* [YHW+25]. Under visible-light irradiation, a sacrificial electron donor, and a Pt cocatalyst, the material exhibited substantial hydrogen evolution. Its reported activity establishes the existence of at least one DBC–cyano-vinylene framework for which the combined conditions

$$\begin{aligned} &\text{light absorption} \\ &+\text{charge migration} \\ &+\text{Pt-directed electron transfer} \\ &+\text{proton reduction} \end{aligned}$$

are experimentally compatible.

The DBC result is used here as a feasibility benchmark, not as an identity relation. The finite DBC fragment $\mathfrak{K}_f$ and rectangular chrysene fragment $\mathfrak{R}_{2,y,f}$ differ in node constitution, attachment coefficients, bridge length, boundary termination, and finite-size symmetry. Moreover, the reported DBC material is an extended solid containing morphology, pores, interlayer interactions, defects, solvent, and heterogeneous Pt sites that are absent from the present calculations. Consequently,

$$\begin{aligned} &\text{electronic similarity to } \mathfrak{K}_f \\ \not\Rightarrow\ &\text{equal hydrogen-evolution activity.} \end{aligned}$$

The justified comparison is narrower: whether the proposed chrysene fragment possesses a nonzero, directionally resolved excited-state polarization that does not contradict the electronic feasibility represented by the benchmark.

A.3 Exciton binding and charge-separation energetics

For a molecular or finite-framework fragment, the fundamental gap may be defined from electron-removal and electron-addition energies as

$$E_{\mathrm{fund}} = I - A,$$

where I is the vertical ionization energy and A is the vertical electron affinity. If E_{opt} is the lowest relevant optical excitation, an effective exciton-binding estimate is

$$E_b = E_{\mathrm{fund}} - E_{\mathrm{opt}}.$$

A positive E_b indicates that the bound optical excitation lies below the free electron–hole threshold within the chosen model. It does not, by itself, determine whether an interface, electric field, solvent, cocatalyst, or structural asymmetry can dissociate the excitation.

For a donor–acceptor partition, a commonly used energetic estimate has the form

$$\Delta G_{\mathrm{CS}} = E_{\mathrm{ox}}(D) - E_{\mathrm{red}}(A) - E_{00} - E_{\mathrm{Coul}},$$

subject to the sign conventions and solvation model used for the individual terms. The condition

$$\Delta G_{\mathrm{CS}} < 0$$

is a thermodynamic admissibility criterion. It is not established by the neutral excited-state calculation reported in this paper because vertical cation and anion energies, relaxed charge-separated states, dielectric stabilization, and interfacial Pt states have not yet been evaluated.

The literature therefore supports a hierarchy of increasingly strong claims:

$$\begin{aligned} &\text{optically accessible excitation,} \\ &\text{spatial polarization,} \\ &\text{thermodynamically favorable charge separation,} \\ &k_{\mathrm{CS}} > k_{\mathrm{rec}}, \\ &\text{electron extraction by Pt,} \\ &R_{\mathrm{H}_2} > 0. \end{aligned}$$

The present calculation addresses only the first two members of this hierarchy.

A.4 Transition-density and charge-transfer diagnostics

An excited state is not adequately characterized by its excitation energy and oscillator strength alone. Natural transition orbitals compress the one-particle transition density into dominant hole–particle pairs [Mar03]. Attachment and detachment densities provide a related real-space description of electron depletion and accumulation [HGGMW95]. Fragment-resolved transition-density approaches can further distinguish local excitation, exciton delocalization, and charge-transfer character [PL12, PWD14].

For normalized detachment and attachment densities $\rho_h(\mathbf{r})$ and $\rho_e(\mathbf{r})$, representative diagnostics include the centroid displacement

$$d_{eh} = \left| \int \mathbf{r}\, \rho_e(\mathbf{r})\, d\mathbf{r} - \int \mathbf{r}\, \rho_h(\mathbf{r})\, d\mathbf{r} \right|$$

and the density-overlap functional

$$\Lambda_{eh} = \int \sqrt{\rho_e(\mathbf{r})\rho_h(\mathbf{r})}\, d\mathbf{r}.$$

A nonzero d_{eh} establishes polarization of the selected state within the chosen finite-fragment model. It does not establish complete charge transfer. Conversely, a small centroid separation does not exclude a spatially extended transition if symmetry causes different contributions to cancel. Centroid, overlap, fragment population, and orbital-pair diagnostics should therefore be interpreted jointly.

This qualification is important for the rectangular chrysene fragment. Its computed directional response is evidence of weak excited-state polarization, not evidence of an isolated electron and hole or a long-lived charge-separated state.

A.5 Range-separated TDA/TD-DFT and methodological limitations

Approximate time-dependent density-functional methods can substantially underestimate the energies of long-range charge-transfer states when the exchange-correlation approximation lacks the required nonlocal exchange behavior [DWHG03]. CAM-B3LYP introduces a distance-dependent partition of exchange intended to improve the description of excitations with long-range character [YTH04]. The Tamm–Dancoff approximation retains the excitation block of the linear-response problem and can improve numerical stability in systems containing problematic de-excitation contributions [HHG99].

These methodological considerations justify the use of CAM-B3LYP/TDA as a screening calculation, but they do not eliminate the effects of basis incompleteness, finite-fragment termination, omitted environmental polarization, geometry uncertainty, state truncation, or functional dependence. In particular, the STO-3G basis used here is insufficient for a quantitative description of diffuse charge-transfer states, electron affinities, or Pt-directed extraction. The calculated roots are therefore treated as intermediate admissibility evidence whose persistence must be tested with larger and more flexible basis sets.

The initial structures were conditioned using the GFN2-xTB method [BEG19] together with the ALPB implicit-solvation model [ESSG21]. These methods provide an efficient preliminary description of large organic fragments but are not substitutes for high-level excited-state optimization or explicit-solvent sampling. The electronic calculations were performed with the PySCF framework [SBB+18], which supports reproducible construction and analysis of the density-fitted range-separated TDA problem.

A.6 Unresolved gap addressed by the present work

The cited literature establishes four relevant precedents:

1. conjugated organic frameworks can support Pt-assisted sacrificial hydrogen evolution;
2. node and bridge chemistry can regulate photocatalytic behavior;
3. donor–acceptor organization and reduced exciton binding can improve charge-separation performance; and
4. a DBC-based cyano-vinylene kagome framework provides a direct chrysene-family experimental benchmark.

None of these precedents establishes that a 3,6,9,12-connected rectangular substituted-chrysene network possesses favorable charge-separation energetics or produces hydrogen. The contribution of the present work is correspondingly limited: it tests whether a range-separated finite-fragment calculation identifies a nonzero and directionally asymmetric excited-state response in the candidate geometry.

The resulting observation provides a rational basis for proceeding to the next computational gates,

$$E_b, \qquad \Delta G_{\mathrm{CS}}, \qquad k_{\mathrm{CS}}/k_{\mathrm{rec}}, \qquad \Delta G_{\mathrm{Pt}},$$

but it cannot replace them. Experimental hydrogen evolution remains contingent on the subsequent satisfaction of these energetic and kinetic conditions and on successful synthesis, catalyst loading, interfacial organization, and reaction testing.

A.7 Chrysene Formalism, Intellectual-Property Provenance, and Prior Benchmark Analysis

Three prior works provide the theoretical, technological, and analytical background for the present study. They serve different evidentiary functions and should not be interpreted as interchangeable forms of validation.

Schaper's *Foundations of the Chrysene Formalism* develops an abstract mathematical framework for representing substituted-chrysene architectures using discrete state spaces, operator algebras, and topological and cohomological structures [Sch26b]. Within this framework, molecular nodes, substitution sites, connecting bridges, and admissible transformations can be treated as components of an encoded network rather than as unrelated molecular structures. This representation motivates the use of specified attachment locants and direction-dependent connectivity in the present rectangular-network model. The monograph supplies a theoretical language for constructing and analyzing candidate architectures; it does not, by itself, establish their synthetic accessibility or photochemical performance.

U.S. Patent No. 12,195,423 describes encoded-design and integrated-synthesis concepts involving substituted-chrysene-derived molecular architectures [Sch25]. In the present context, the patent documents the technological and intellectual-property provenance of the broader substituted-chrysene platform. A patent grant, however, is not evidence that a particular network performs charge separation, transfers an electron to a cocatalyst, or evolves hydrogen. Those questions require separate computational and experimental tests.

The most directly relevant analytical precursor is the conditional comparison of a 3,6,9,12-connected rectangular chrysene network with a dibenzochrysene-based kagome photocatalyst benchmark [Sch26a]. That study introduced matched bridge and Pt-assisted sacrificial hydrogen-evolution conventions and examined geometric density, direction-dependent electronic coupling, lattice spectra, transport, charge-separation admissibility, and kinetic competition. Its principal result was conditional: if the specified energetic, coupling, extraction, and kinetic inequalities hold, the rectangular architecture is not mathematically excluded from supporting Pt-assisted hydrogen evolution. In particular, nonvanishing directional couplings,

$$T_x T_y \neq 0,$$

establish electronic communication in the reduced lattice model but do not independently prove

$$\Delta G_{\mathrm{CS}} < 0, \qquad k_{\mathrm{CS}} > k_{\mathrm{rec}}, \qquad \text{or} \qquad R_{\mathrm{H}_2} > 0.$$

The present study addresses part of this remaining evidentiary gap by replacing purely effective network elements with explicit finite molecular fragments and by applying range-separated electronic-structure calculations and spatial population diagnostics. The relationship among the works may therefore be summarized as

$$\begin{aligned}
\text{mathematical formalism} &\longrightarrow \text{encoded candidate architecture},\\
\text{patent disclosure} &\longrightarrow \text{technological and IP provenance},\\
\text{conditional benchmark} &\longrightarrow \text{necessary network-level criteria},\\
\text{present calculation} &\longrightarrow \text{molecular testing of selected criteria}.
\end{aligned}$$

Together, these references motivate the candidate architecture and define the questions to be tested, while the photophysical and catalytic claims remain subject to progressively higher-level calculation and prospective experimental falsification.

Data and Code Availability

The molecular-structure files, calculation inputs, intermediate and final numerical outputs, and analysis code supporting this study are available from the corresponding author upon reasonable request submitted through the editorial office of the *Annals of the Chrysene Formalism*. The available materials are intended to permit reconstruction of the finite fragments, verification of the reported electronic-structure calculations, and reproduction of the population and admissibility analyses.

References

[BEG19] Christoph Bannwarth, Sebastian Ehlert, and Stefan Grimme. GFN2-xTB—an accurate and broadly parametrized self-consistent tight-binding quantum chemical method with multipole electrostatics and density-dependent dispersion contributions. *Journal of Chemical Theory and Computation*, 15(3):1652–1671, 2019.

[DWHG03] Andreas Dreuw, Jennifer L. Weisman, and Martin Head-Gordon. Long-range charge-transfer excited states in time-dependent density functional theory require non-local exchange. *The Journal of Chemical Physics*, 119(6):2943–2946, 2003.

[ESSG21] Sebastian Ehlert, Marcel Stahn, Sebastian Spicher, and Stefan Grimme. Robust and efficient implicit solvation model for fast semiempirical methods. *Journal of Chemical Theory and Computation*, 17(7):4250–4261, 2021.

[HGGMW95] Martin Head-Gordon, Ana M. Graña, David Maurice, and Christopher A. White. Analysis of electronic transitions as the difference of electron attachment and detachment densities. *The Journal of Physical Chemistry*, 99(39):14261–14270, 1995.

[HHG99] So Hirata and Martin Head-Gordon. Time-dependent density functional theory within the tamm–dancoff approximation. *Chemical Physics Letters*, 314(3–4):291–299, 1999.

[IAY+22] Tomoya Imai, Ryuhei Akasaka, Naruhiro Yoshida, Toru Amaya, and Tetsuo Iwasawa. Electrochemical and spectroscopic properties of twisted dibenzo[g,p]chrysene derivatives. *Beilstein Journal of Organic Chemistry*, 18:963–971, 2022.

[LLL+22] Chunzhi Li, Jiali Liu, He Li, Kaifeng Wu, Junhui Wang, and Qihua Yang. Covalent organic frameworks with high quantum efficiency in sacrificial photocatalytic hydrogen evolution. *Nature Communications*, 13(1):2357, 2022.

[Mar03] Richard L. Martin. Natural transition orbitals. *The Journal of Chemical Physics*, 118(11):4775–4777, 2003.

[PAR+18] Pradip Pachfule, Amitava Acharjya, Jérôme Roeser, Thomas Langenhahn, Michael Schwarze, Reinhard Schomäcker, Arne Thomas, and Johannes Schmidt. Diacetylene functionalized covalent organic framework (COF) for photocatalytic hydrogen generation. *Journal of the American Chemical Society*, 140(4):1423–1427, 2018.

[PL12] Felix Plasser and Hans Lischka. Analysis of excitonic and charge transfer interactions from quantum chemical calculations. *Journal of Chemical Theory and Computation*, 8(8):2777–2789, 2012.

[PWD14] Felix Plasser, Michael Wormit, and Andreas Dreuw. New tools for the systematic analysis and visualization of electronic excitations. i. formalism. *The Journal of Chemical Physics*, 141(2):024106, 2014.

[SBB+18] Qiming Sun, Timothy C. Berkelbach, Nick S. Blunt, George H. Booth, Sheng Guo, Zhendong Li, Junzi Liu, James D. McClain, Elvira R. Sayfutyarova, Sandeep Sharma, Sebastian Wouters, and Garnet Kin-Lic Chan. PySCF: The python-based simulations of chemistry framework. *WIREs Computational Molecular Science*, 8(1):e1340, 2018.

[Sch25] Charles D. Schaper. Encoded design integrated synthesis of nucleic acids, and phospholipids, and related pharmaceutical products, 2025. Patent US 12,195,423.

[Sch26a] Charles D. Schaper. Electronic and kinetic feasibility of a 3, 6, 9, 12-connected rectangular chrysene network for pt-assisted hydrogen evolution: A conditional comparison with a dibenzochrysene kagome benchmark. *Annals of the Chrysene Formalism*, 1(1):365–387, 2026.

[Sch26b] Charles D. Schaper. *Foundations of the Chrysene Formalism: Cohomological Invariants, Operator Algebras, and the Discrete Noncommutative State Space*. Schaper Systems Press, San Francisco, CA, 2026. ISBN: 979-8-950371-08-0.

[VHS+15] Vijay S. Vyas, Frederik Haase, Linus Stegbauer, Gökcen Savasci, Filip Podjaski, Christian Ochsenfeld, and Bettina V. Lotsch. A tunable azine covalent organic framework platform for visible light-induced hydrogen generation. *Nature Communications*, 6:8508, 2015.

[WCC+18] Xiaoyan Wang, Linjiang Chen, Samantha Y. Chong, Marc A. Little, Yongzhen Wu, Wei-Hong Zhu, Rob Clowes, Yong Yan, Martijn A. Zwijnenburg, Reiner Sebastian Sprick, and Andrew I. Cooper. Sulfone-containing covalent organic frameworks for photocatalytic hydrogen evolution from water. *Nature Chemistry*, 10(12):1180–1189, 2018.

[YHW+25] Jun-Jie Yu, Xin Huang, Li-Ying Wang, Yan-Ze Wu, Zhi-Wei Huang, Ling-Ling Su, Nan-Nan Wang, Ji-Pan Yu, and Wei-Qun Shi. Topology-templated synthesis of dibenzo[g,p]chrysene-based sp^2 carbon-linked covalent organic frameworks with kagome lattice for enhanced photocatalytic hydrogen evolution. *Advanced Materials*, 37(44):e04808, 2025.

[YTH04] Takeshi Yanai, David P. Tew, and Nicholas C. Handy. A new hybrid exchange–correlation functional using the coulomb-attenuating method (CAM-B3LYP). *Chemical Physics Letters*, 393(1–3):51–57, 2004.